Do upper-plate material properties or fault frictional properties dominate tsunami earthquake characteristics?

Qingjun Meng[1], Benchun Duan[1*]

(1) Center of Tectonophysics, Department of Geology & Geophysics, Texas A&M University, College Station, TX, United States.

Corresponding author: Benchun Duan (bduan@tamu.edu)

Abstract

Tsunami earthquakes are a type of shallow subduction zone events that rupture slowly (<1.5 km/s) with exceptionally long duration and depleted high frequency radiation, resulting in a large discrepancy of *Mw* and *Ms* magnitudes and abnormally large tsunami along coastal areas. Heterogeneous fault frictional properties at shallow depth have been thought to dominate tsunami earthquake generation. Some recent studies propose heterogeneous upper-plate material properties determine rupture behavior of megathrust earthquakes, including characteristics of tsunami earthquakes. In this study, we use a recently developed dynamic earthquake simulator to explore tsunami earthquake generation and systematically examine roles of upper-plate material properties and fault frictional properties in tsunami earthquake characteristics in a physics-based framework. For heterogeneous fault friction, we consider isolated asperities with strongly velocity-weakening properties embedded in a conditionally stable zone with weakly velocity-weakening properties. For heterogeneous upper-plate properties, we consider a generic depth profile of seismic velocity and rigidity constrained from seismic surveys. We design a set of models to explore their effects on tsunami earthquake generation and characteristics. We find that the conditionally stable zone can significantly slow down rupture speeds of earthquakes that nucleate on asperities to be < 1.5 km/s over a large depth range (1-20 km), while heterogeneous upper-plate properties can only reduce rupture speeds to be ~1.5-2.0 km/s over a narrow depth range (1-3km). Nevertheless, heterogeneous upper-plate properties promote cascading rupture over multiple isolated asperities on the shallow subduction plane, contributing to large tsunami earthquake generation. We also find that heterogeneous friction dominates normalized duration and high-frequency depletion in tsunami

earthquakes. In addition, the effective normal stress on the subduction plane, which affects fault frictional strength, significantly influences the characteristics of tsunami earthquakes, including long normalized duration and low stress drop.

Key words: tsunami earthquakes, fault friction, upper-plate material, effective normal stress, rupture speed, normalized duration

1. Introduction

Tsunami earthquakes are interplate earthquakes along shallow subduction zones that generate much larger tsunami than their surface wave magnitude (*Ms*) could imply (Kanamori, 1972). There have been a number of well-studied tsunami earthquakes, including the 1992 Nicaragua earthquake (Kanamori and Kikuchi, 1993), the 1994 Java earthquake (Abercrombie *et al*., 2001; Bilek and Engdahl, 2007), the 1996 Peru earthquake (Ihmlé *et al*., 1998), the 2006 Java earthquake (Ammon *et al*., 2006; Bilek and Engdahl, 2007), and the 2010 Mentawai earthquake (Lay *et al*., 2011), listed in Table S1 together with some earlier events. Compared to ordinary earthquakes, tsunami earthquakes have slow rupture speeds around 1.5 km/s or slower, abnormally long duration (e.g., 185 s for Java 2006 event), and source spectra depleted in short-period energy, resulting in large discrepancy between their *Ms* and *Mw* magnitudes (e.g., *Ms* 7.2 vs *Mw 7.8* for Java 2006 event). They usually occur along the shallow portion (e.g., < 15 km depth) of subduction interfaces.

A conceptual model based on the rate- and state-dependent fault friction has been proposed to understand tsunami earthquake generation. For example, Bilek and Lay (2002) studied both large tsunami earthquakes and smaller shallow subduction zone earthquakes and found that they all have longer normalized duration compared with deeper earthquakes (> 15km). They proposed that these earthquakes are associated with ruptures on locally locked unstable patches (asperities) within largely conditionally stable zones over shallow subduction interfaces. Frictional stability regimes over subduction interface are typically defined in the framework of the rate- and state-dependent friction law, including stable zones where fault slips stably without seismic radiation, unstable zones where seismic slip occurs, and conditionally stable zones where slip is generally stable but earthquakes can propagate through them at slow speeds (Scholz, 1998). Bilek and Lay (2002) proposed that the locally locked unstable patches may be related to subducted seamounts, ridges and host and graben structure, which could produce roughness on subduction zone interfaces. The conditionally stable zone could be a transition zone between the shallow velocity strengthening area (aseismic) and the downdip velocity weakening area (seismic). There are different mechanisms explaining this transition. Early studies proposed that the transition of smectite clays to illite and chlorite, when smectite gets dehydrated as temperature increases with depth, could trigger a change from velocity strengthening to velocity weakening (Wang, 1980; Hyndman and Wang, 1993; Hyandman *et al*., 1997). Saffer *et al.* (2012) proposed that mineral precipitation, for example calcite and quartz, and shear localization could function in driving the frictional transition and the heterogeneity of fault frictional behavior.

Recently, Sallares and Ranero (2019) proposed that, without the necessity to consider fault mechanics, depth-dependent upper-plate elastic properties determine depth-varying rupture characteristics, including larger slip, slower rupture speed and depletion of high frequency energy for earthquakes at the shallow domain (depth< 5 km) than those at the deep domain (depth>10 km).

Prada *et al*. (2021) performed 3D dynamic rupture modeling to assess the difference in rupture behaviors between the shallow and deep domains, adopting a slip-weakening law with essentially uniform fault friction properties on the fault plane. They concluded that a depth-dependent upper plate rigidity explains most of the observed seismological behaviors of both tsunami earthquakes and large megathrust earthquakes.

There are several concerns about the dominant role of the depth-dependent upper-plate property for tsunami earthquake generation advocated in these recent studies. First, without comparing roles of the upper-plate elastic property and the fault frictional property in one physics-based framework, it is premature to conclude which one plays a more important role in tsunami earthquake generation. Second, the rupture speed, which is constrained to be lower than S wave velocity (*Vs*) at each depth in their mechanism, is relatively small (~1.5 km/s) only at top 3 km depth, while below 5 km depth rupture speed is larger than 2 km/s (e.g., Figure 6e in Prada *et al*., 2021). This very narrow depth range (< 3 km) of slow rupture speed is not comparable to the observed range of centroid depth for historical tsunami earthquakes, which is up to 10 km (Bilek and Lay, 2002) or even to 15 km (Abercrombie *et al*., 2001). Complemental to the rupture speed, the normalized duration of earthquakes is a good measurement to compare duration of earthquakes of different sizes (*Mw*). Prada *et al*. (2021) did not calculate normalized durations of simulated earthquakes in their models and thus did not compare with those from observed tsunami earthquakes. Third, Prada *et al.* (2021) applied a 1D velocity structure constrained only for the upper plate from seismic data (Sallares and Ranero, 2019) to both the upper plate (hanging wall) and the under-thrusting plate (footwall) in their heterogeneous velocity model. They mainly compared this heterogeneous model to a homogeneous model to examine the dominant role of the upper-plate elastic property. When using a bimaterial model in which the 1D velocity structure in the hanging wall and a uniformly high velocity in the footwall are adopted, the rupture speed in their results (Figure 9c in Prada *et al*., 2021) at shallow depth is much higher than that from their heterogeneous model, diminishing the effect of slowing down rupture by the upper-plate low-velocity layers at shallow depth.

In this study, we examine effects of the upper-plate elastic property and the fault frictional property on tsunami earthquake characteristics in one physics-based framework using a 3D fully dynamic earthquake simulator (Luo *et al*, 2020; Meng *et al*., 2022). We build a heterogeneous velocity structure model in which the upper-plate 1D velocity structure from Sallares and Ranero (2019) for the hanging wall is combined with a two-layer velocity structure for the footwall to examine roles of heterogeneous upper-plate properties. For roles of the fault frictional property, we consider two asperities with strongly velocity-weakening friction properties embedded in a conditionally stable zone with weakly velocity-weakening friction properties on a shallow subduction interface. Together with other models in which either simpler velocity structure or simpler friction distribution is adopted, we compare and contrast roles of heterogeneous upper-plate properties and heterogeneous fault friction properties in tsunami earthquake generation and characteristics. We utilize a fully dynamic earthquake cycle simulator to run all models. We examine the rupture speed variance, normalized duration, slip, stress drops and frequency contents from the models and compare them with those observed from historical tsunami earthquakes. We find that heterogeneous fault frictional properties dominate tsunami earthquake characteristics.

2. Method

In this study, we use a fully dynamic earthquake simulator (Luo *et al.*, 2020; Meng *et al.*, 2022) to simulate slip behaviors of a shallow-dipping subduction interface over multiple earthquake cycles, including the coseismic, postseismic, interseismic, and nucleation phases. Unlike single-event dynamic rupture modeling, the multicycle dynamic simulations allow us to examine rupture characteristics of a sequence of dynamic events for a given set of model parameters. In particular, the initial stress condition for a dynamic event later in the sequence takes into account the effects of previous earthquake cycles, including previous dynamic events. The dynamic simulator is based on an explicit finite element method (FEM) code EQdyna that was developed for dynamic rupture simulations and has gone through multiple benchmark tests (Duan and Oglesby, 2006; Duan and Day, 2008; Duan, 2010; Duan, 2012; Luo and Duan, 2018; Liu and Duan, 2018). The dynamic earthquake simulator directly uses EQdyna to simulate coseismic dynamic processes, and integrates EQdyna with an adaptive dynamic relaxation technique (Qiang, 1988) and a variable time stepping scheme (Lapusta *et al.*, 2000) to simulate the quasi-static processes, including postseismic, interseismic, and nucleation phases. Thus, both dynamic and quasi-static processes are simulated within the same FEM framework. The quasi-static processes transition to dynamic processes when the maximum slip rate is larger than an empirical threshold V_{th1}=0.01 m/s, and the dynamic processes transition to quasi-static processes when the maximum slip rate is smaller than an empirical threshold value V_{th2}=0.005 m/s (Luo *et al.*, 2020; Meng *et al.*, 2022). On the plate interface, a commonly used rate-and state-dependent friction (RSF) law with aging law (Dieterich, 1979) is adopted (e.g., Lapusta *et al.*, 2000; Lapusta and Liu, 2009), as shown by equations:

$$\tau = \sigma * (f_0 + a\, ln\frac{V}{V_0} + b\, ln\frac{V_0\theta}{L}) \qquad (1)$$

$$\frac{d\theta}{dt} = 1 - \frac{V\theta}{L} \qquad (2)$$

The friction strength τ is controlled by effective normal stress σ, reference friction coefficient f_0, parameters a and b, slip rate V, reference slip rate V_0, state variable θ and critical slip distance L. The friction strength, effective normal stress, slip rate and state variable will evolve through time automatically from their initial values based on equations (1)(2), while other parameters a, b, f_0 and L are fixed throughout multiple cycles. The friction strength is both rate dependent and state dependent, which is controlled by the friction parameters a and b. When a-b > 0, the fault plane is velocity strengthening and slip tends to be stable. When a-b < 0, the fault plane is velocity weakening, and slip can be either unstable or conditionally stable (Scholz, 1998; Liu and Rice, 2007), depending on the ratio of H/h*, where H is the fault width (the smaller dimension along strike and dip) and h* is the critical nucleation size. When H is larger than h*, slip is unstable and earthquake can both nucleate and propagate. When H is equal or smaller than h*, slip is conditionally stable and earthquake can propagate but not nucleate in this zone. The critical nucleation size h* depends on multiple parameters, and an estimate of the nucleation size h^* for 3D mode II earthquakes (Chen and Lapusta, 2009; Rubin and Ampuero, 2005) is:

$$h^* = \frac{\pi}{2}\frac{\mu b L}{(1-\nu)(a-b)^2\sigma} \qquad (3)$$

where a, b, σ and L are the same parameters as in equation (1), ν is Poisson's ratio and μ is shear modulus.

3. Models

We set up 3D models with a dipping angle ϕ= 20° and the model dimension is shown in Figure 1a, with other basic parameters shown in Table S2. Because we focus on studying the shallow tsunami earthquakes, the main fault plane only extends to ~22 km in depth. The top boundary of the model is free surface (Z=0), while the left (X=Xmin) and right (X=Xmax) boundaries are fixed along X direction, $u_x = 0$. Other boundaries (Y=Ymin, Y=Ymax and Z=Zmin) are assigned with a loading rate of $0.5*V_{pl}$=0.5x10^{-9} m/s parallel with the fault interface, to make the footwall to move downward and the hanging wall to move upward parallel with the fault plane. In these FEM models, we mainly use hexahedral elements for computation efficiency, while near the fault interface we cut a hexahedral element to two wedge elements to conform the shallow-dipping geometry, using the degeneration technique (Hughes, 2000; Duan, 2010; Duan, 2012; Luo and Duan, 2018). The thrust fault intersects with free surface with a generally velocity weakening main fault plane surrounded by the velocity strengthening creeping area.

We design a set of models to systematically examine the effects of heterogeneous upper-plate velocity structure and heterogeneous fault friction on tsunami earthquake generation and characteristics. We have two velocity structure models (a simple model and a heterogeneous model) and two friction-distribution models (a uniform model and a nonuniform model). The simple velocity model applies two-layer velocity structure in both the hanging wall and footwall (Figure 1b). The two-layer structure, with a thin top layer overlying a half-space bottom layer, is a simplified structure of the upper part of subduction zone under-thrusting plate (Contreras-Reyes *et al*., 2017). The top layer (<2 km) has lower velocity *Vp*=5 km/s and *Vs*=2.5 km/s and the bottom layer has slightly higher velocity *Vp*=6.0 km/s and *Vs*=3.5km/s. The heterogeneous velocity model adopts the 1D depth-dependent velocity structure from Sallares and Ranero (2019) for the hanging wall and the two-layer structure for the footwall (Figure 1c). The 1D depth-dependent velocity structure is based on the upper-plate P-wave velocity obtained with travel-time modelling of seismic profiles across circum-Pacific and Indian Ocean subduction zones (Sallares and Ranero, 2019), within which the velocity and density at shallow depth drop significantly compared to those at deeper depth, implying a much more complaint prism than the simple velocity model. For the uniform friction model, the friction parameters a, b, critical distance, and effective normal stress are shown in Figure 2. Over most of the fault plane the a-b value is strongly velocity weakening with a value of -0.004, while a-b gradually increases from -0.004 at 4 km depth to 0.008 at the trench (Figure 2f). Friction parameter a-b also gradually increases to positive values on other three edges of the main fault plane (Figure 2c). We denote this friction distribution as the uniform friction model though friction parameters are not strictly uniform on the main fault plane. The effective normal stress is 50 MPa below 4km depth (assuming overpressurization of pore fluid) and gradually reduces to 5 MPa near the trench (Figure 2g). For the nonuniform friction model, the friction parameters a, b, critical distance, and effective normal stress are shown in Figure 3. Below 4km depth, the a-b equals -0.0015 (weakly velocity weakening) over the conditionally stable zone, while a-b equals to -0.004 (strongly velocity weakening) over two asperities (Figure 3c and 3f). The effective normal stress on the conditionally stable zone is 50 MPa and over two asperities Z1 and Z2 is 90 MPa (80% higher than the conditionally stable zone) and 70 MPa (40% higher than the conditionally stable zone) respectively, where Z1 is a high normal stress (HNS) asperity and Z2 is a low normal stress (LNS) asperity.

There are four main models with different combinations of the two velocity models (simple vs heterogeneous) and the two friction models (uniform vs nonuniform) (Table 1). Models 1 and 3 utilize the simple velocity model, while Models 2 and 4 apply the heterogeneous velocity model. Models 1 and 2 utilize the uniform friction model on the fault plane, while Models 3 and 4 utilize the nonuniform friction model. Previous studies find that fluid overpressurization could give rise to low effective normal stress along subduction zones (Kitajima & Saffer, 2012; Bassett *et al*., 2014; Kimura *et al*., 2012) and we build Model 5 with low effective normal stress to examine its effect. Model 5 uses the heterogeneous velocity model and the nonuniform friction model, similar to Model 4. The main difference comes from the low effective normal stress on the conditionally stable zone (30 MPa) and on two asperities (42 MPa, 40% higher than conditionally stable zone) (Figure S1). In Model 5, the average normal stress over the whole fault plane is lower than that in Models 1-4 (~60%).

We calculate the h* value for all models based on equation (3) (Figure S2 and S3). In this study, h* is used as a reference to determine whether the fault plane is unstable (H>h*) or conditionally stable (H=<h*). In the uniform friction model, the fault width is much larger than the h* over the fault plane, where earthquakes can both nucleate and propagate (Figure S2). In the nonuniform friction model, the size of asperities is large than h* on them and earthquake could nucleate and propagate on them while the width of conditionally stable zone is smaller than h* on it, so that earthquakes cannot nucleate but can propagate on it. In addition, h* is not only related with friction parameters (a, b, σ and L), but also related with shear modulus μ (μ=$\rho * V_s^2$), thus h* for the hanging wall and footwall might be different in the heterogeneous velocity model, shown in Figure S2 and S3.

4. Results

4.1 Earthquake cycles

We simulate three earthquake cycles that include at least three dynamic events for each model (Figure 4). The recurrence intervals of earthquakes range from ~100 years to ~220 years. By comparing the recurrence intervals of all models, we find that the normal stress, which may be considered as a fault plane property as it determines the fault frictional strength (together with the frictional coefficient), plays an important role in determining the recurrence interval. The smallest interval comes from Model 5 (~100 Years), where the normal stress (30 MPa on the conditionally stable zone and 42 MPa on asperities) is much lower than other models. A lower normal stress represents a lower fault strength with other similar friction parameters. When the fault plane is loaded with the same rate for all models, the recurrence interval will be shortened for the model with low fault strength. For Model 1 and Model 2, the recurrence intervals are around 160 years, longer than in Model 5, due to a higher initial normal stress of 50 MPa over the fault plane. The longest interval occurs in Model 4, where normal stress is 50 MPa on the conditionally stable zone, 90 MPa on HNS asperity Z1 and 70 MPa on LNS asperity Z2. In addition, a compliant upper plate also influences the earthquake recurrence interval, comparing Model 3 (interval of ~175 years) and 4 (interval of ~220 years). For Model 3, only the first dynamic event (D1) ruptures both Z1 and Z2 asperities, later events (D2- D4) rupture only part of the fault plane, either Z1 or Z2 asperity. In comparison, for Model 4, every single dynamic event ruptures the whole fault plane including both asperities Z1 and Z2 (Table 1 and Figure 4). In Model 4, the more compliant upper-plate material at shallow depth (Figure 1c) seems to facilitate cascading failures of multiple asperities over the whole fault plane, which results in complete release of elastic energy. Therefore, it takes a longer time to accumulate enough elastic strain for the next event. We calculate the h* value based on the depth dependent velocity structure and the two-layer structure, and find that the low velocity at shallow depth leads to a low rigidity and a smaller h* at shallow depth, shown in Figure S3, where smaller h* could contributes to more unstable failure in Model 4.

In summary, the effective normal stress, which may be considered as a fault property, plays a dominant role in the earthquake recurrence interval. Low effective normal stress shortens, and high effective normal stress elongates the recurrence interval. A compliant upper plate material plays a secondary role in promoting cascading failure and complete energy release when multiple asperities are distributed within the conditionally stable zone, which elongates the recurrence interval.

4.2 Rupture speed

Historical tsunami earthquakes are well known for their unusual slow rupture speeds, typically lower than 1.5 km/s (Pelayo and Wiens, 1992; Ammon *et al.*, 2006; Lay *et al.*, 2011). In this study, we quantitatively calculate the rupture speed for all models to evaluate which factor contributes more to the slow rupture speed. We select the first dynamic event (D1) in each model to plot their rupture time contours, where the rupture time (t_r) is determined by the time when slip rate first reaches the threshold of v_l= 0.01 m/s at each fault node during the dynamic rupture process (Figure 5). Based on the rupture time, we calculate the rupture speed as inverse of rupture slowness (Bizzarri & Das, 2012):

$$v_r(x_s\,, x_d) = \frac{1}{\left\| \nabla_{(x_s\,, x_d)} t_r(x_s\,, x_d) \right\|} \qquad (4)$$

where x_s and x_d are along strike and along dip directions. Because the rupture speed near earthquake nucleation point could be extremely low, we exclude those areas during rupture speed calculation (Figure 5). In addition, we select two along dip (depth) bands to obtain two profiles showing how rupture speed changes at different depth (Figure 5), with one profile closer to the nucleation point (red line) and the other further away (black line).

Generally, the rupture speed is limited to be lower than *Vs* of the hanging wall at each depth, shown in Figure 5. We compare the rupture speeds in Models 1 and 2 to explore the influence from the upper plate property (Figures 5a and 5b). We find that the rupture speed at shallow depth (<10 km) in Model 2 is lower than that in Model 1, because the velocity in the hanging wall is lower in Model 2 than in Model 1 at shallow depth. In Model 2, rupture speed at depth of 1-3km drops to 1.5-2.0 km/s, though still higher than typical tsunami earthquake rupture speed <1.5 km/s and the narrow range (1-3 km) is not consistent with the depth range of historic tsunami earthquakes (<10 km). At the topmost layer (<1km depth), the rupture front encounters the free surface and the rupture speed accelerates to be supershear, larger than *Vs* in the hanging wall. We use rupture speed results in Models 3-5 to study the influence from the fault property (Figure 5c-e), because these models all utilize the nonuniform friction model, with two strong velocity weakening asperities embedded in the conditionally stable zone. The rupture speed over the asperities is still high (2-3km/s), while the rupture speed in the conditionally stable zone effectively drops to be lower than 1.5 km/s, unrelated with depth. The topmost layer (<1km depth) still has some scattered segments of supershear rupture speed. However, supershear zones are not continuous along the trench and are separated by very low rupture speed zones updip of the central conditionally stable zone. Comparing Models 3 and 4, rupture speed over the conditionally stable zone in Model 4 is slightly faster than that in Model 3, which could be related to a more compliant hanging wall and smaller h* in Model 4, shown in Figure S3, making the fault more unstable. In Model 5, the low normal stress on asperities and conditionally stable zone further contributes to slowing down the rupture speed, comparing with that in Model 4.

In summary, the conditionally stable zone in nonuniform fault friction models could significantly contribute to generating an especially low rupture speed below 1.5 km/s at a wide depth range. The upper-plate depth dependent material property mainly contributes to slow rupture speed limited at very shallow depth (e.g., 1-3 km).

4.3 Stress change, slip, moment rate

We compare the stress change, final slip and moment rate function for the first dynamic event of each model in Figure 6. The maximum stress drop and slip come from Models 1 and 2, both of which have strong velocity weakening friction over the fault plane. The maximum final slip is especially high near shallow depth for Model 2 (~16 m), while the maximum final slip for Model 1 is ~12.5 m. This phenomenon is due to the more complaint hanging wall velocity structure in Model 2, consistent with the previous study (Prada *et al.*, 2021). The two models have similar average stress drops (~5.1 MPa) and similar total moments (~$1.0*10^{21}$Nm, ~*Mw* 7.9), which are much higher than those in Models 3-5. Models 3-5 have two separate velocity weakening asperities embedded in the conditionally stable zone. The stress drop and slip are higher near two asperities, while lower in the conditionally stable zone, demonstrating that the conditionally stable zone contributes not only to slow rupture speed but also to low stress drop and final slip. The average stress drops in Models 3 and 4 are ~3.0 MPa and the total moments are also close, $4.06*10^{20}$ Nm (*Mw* 7.68) from Model 3 and $4.49*10^{20}$ Nm (*Mw* 7.71) from Model 4. In Model 5, the average stress drop significantly reduces to ~1.65 MPa due to the low normal stress condition, leading to smaller final slip (maximum 3.5 m) and total moment (2.3*10^{20} Nm, ~ *Mw* 7.5).

To better study stress drop over a sequence of earthquakes over multiple earthquake cycles, we calculate the average stress drops over the whole fault plane, inside asperities and outside asperities (over the conditionally stable zone), for all dynamic events simulated in Models 1-5, shown in Figure S4. Though, the stress drop values may scatter among different dynamic events in each model, it is still obvious that low normal stress in Model 5 contributes to the low average stress drop compared with other models. In Models 3-5, stress drop in the conditionally stable zone is much lower than that in asperities, due to the weakly velocity weakening friction property and low normal stress in the conditionally stable zone. The average stress drop values are also listed in Table 1.

4.4 Normalized moment rate and spectrum

Because the simulated events have different moments, we use the earthquake scaling relations (Kanamori and Anderson, 1975; Vidale and Houston,1993) to normalize the moment rate functions by following Houston *et al*. (1998) and Bilek and Lay (1999) to remove effects of the total moment on the shape of the moment rate function, shown in Figure 7. The normalization can be expressed as

$$\dot{M}_{norm}(t) = \left(\frac{M_{0ref}}{M_0}\right)^{\frac{2}{3}} \dot{M}(\tau)\ ,\ \ t = \left(\frac{M_{0ref}}{M_0}\right)^{\frac{1}{3}} \tau \quad (5),$$

where τ is the original time, t is the normalized time, M_0 is the total moment of the event, M_{0ref} is the seismic moment of a reference earthquake (*Mw* 6 used in this study), $\dot{M}(\tau)$ is the original moment rate function and $\dot{M}_{norm}(t)$ is the normalized moment rate function.

To avoid overestimation of source duration due to the low moment rate at the early and late stages of a simulated event, we use a threshold of moment rate > 10^{17} Nm/s, about the moment rate of a M_w 5.5 earthquake, to determine the starting and ending times in $\dot{M}(\tau)$ for source duration measurements (Figure 6). The source duration of the normalized moment rate function is defined as the normalized duration for the event. We measure the normalized durations of all simulated events as listed in Table 1 and Figure S5 and compare them with those observed from historical tsunami earthquakes. The normalized duration of observed historical tsunami earthquakes ranges from 9 to 23 s (Table S1), much larger than deeper megathrust earthquakes of around 5 s (Bilek and Lay, 2002). The simulated events in Models 3 and 5 of this study have larger normalized durations (> 10s) than those from other models, primarily due to the low rupture speed in the conditionally stable zone. For Model 5 (low normal stress), the exceptionally long normalized duration (e.g., 14 s for D2) is further related with the low normal stress. The normalized duration is proportional to duration and cube root of moment, $T/M_0^{1/3}$. A low normal stress leads to a lower total moment M_0. Therefore, a slightly longer source duration T, shown in Figure S6, leads to a significantly longer normalized duration in this event. However, the events simulated in Model 2 (compliant upper plate) only have slightly increased normalized durations compared to those in Model 1. This is because the compliant upper plate mainly slows down the ruptures at 1-3 km depth with minor effects on the deeper part of the subduction plane. In addition, the normalized duration in Model 4 is shorter than in Model 3 due to the influence of the compliant upper plate in Model 4. As discussed earlier, dynamic events tend to rupture a series of asperities more smoothly in a cascade fashion with a faster rupture speed due to the compliant upper plate.

Based on the normalized moment rate functions, we calculate and compare the spectrum of all simulated events D1, shown in Figure 8. In Models 3-5, the spectra have much lower corner frequency (where moment starts to reduce) and are more depleted of high frequency energy compared with spectrum in Model 1, under the influence of nonuniform friction. Such phenomena are consistent with common features of historical tsunami earthquakes. However, for Model 2, the corner frequency is nearly the same with that in Model 1, implying a very weak effect on corner frequency reduction from the compliant upper plate in this study.

4.5 Seafloor displacement (Model 5)

In this study, we regard the dynamic events simulated in Model 5 as typical examples of tsunami earthquakes. Taken event D2 as an example (*Mw* 7.5, normalized duration of 14 s), we output the seafloor vertical and horizontal displacements to estimate its tsunami generation potential, shown in Figure 9ab. This *Mw* 7.5 event with centroid depth near 10 km could cause a permanent vertical ground surface displacement up to 1m and horizontal displacement more than 2 m. Large seafloor displacement occurs over a large area of 70 km (along trench) by 30 km (perpendicular to trench). An observed tsunami earthquake with similar magnitude and centroid depth is the Peru 1975 *Mw* 7.5 event, which led to tsunami runups of several meters in some coastal areas (Ihmle *et al*., 1998). This historical event demonstrates that tsunami earthquakes could occur as deep as 10 km and cause unneglectable tsunami hazard. We plot the continuous waveforms of seafloor displacement for stations within a virtual array located over the hanging wall (Figure 9c). The displacement waveforms are complex and the stations to the left side (X< 0 km) show two displacement runup stages. This complexity is related with the noncontinuous rupture of multiple asperities in the nonuniform friction model. In addition, we find that two stations (A and B) near the trench have larger displacement than other near trench stations (Figure 9c). Based on the final slip distribution over fault plane (Figure S6), two places on the subduction plane below stations A and B have larger slip than other near trench area. From the rupture speed distribution (Figure S7), a strong variation of rupture speed occurs along strike at shallow depth, with high speed (supershear, > 2km/s) near stations A and B and low speed (<<1 km/s) between stations A and B. This results in a low average rupture speed from station A to station B of below 1 km/s (Figure S8), despite that the rupture speed near station A and B locally exceeds shear wave velocity. In fact, these places (near stations A and B) of high rupture speed, large final slip and large seafloor displacement locate updip of the two asperities (at depth of 10 km).

5. Discussion

In this study, we explore whether the upper-plate velocity structure or the fault friction is more important in tsunami earthquake generation and characteristics. We find that in the models with the nonuniform friction distribution, the conditionally stable zone can effectively slow down rupture speed to be lower than 1.5 km/s (typical tsunami earthquake rupture speeds), no matter what velocity structure is used. Correspondingly, the nonuniform friction distribution also contributes to long normalized duration, low corner frequency and high frequency energy depletion, consistent with the features observed from historical tsunami earthquakes. The heterogeneous upper-plate velocity structure is not sufficient to slow down the rupture speed to be <1.5 km/s even at very shallow depth

(<3 km), when the uniform friction distribution is applied on the main fault plane (Model 2). Furthermore, the normalized duration elongation, corner frequency reduction and high frequency energy depletion effects (for simulated events at ~10 km centroid depth) are all neglectable in this model. The most significant contribution from the heterogeneous upper-plate velocity structure is the enhancement of slip near trench, as shown in comparison between Models 1 and 2. Generally, the factors of strong velocity weakening, high normal stress and compliant upper plate in Model 2 contribute to large moment release rate and large final slip near trench, which could generate large seafloor displacement and fatal tsunami waves. On the contrary, the factors of conditionally stable zone, low normal stress and compliant upper plate in Model 5 contribute to slow rupture speed, slow moment release rate, depletion of high frequency energy and enhanced slip near shallow depth. We propose tsunami earthquakes more likely occur in subduction zones with on-fault property and upper-plate property similar to Model 5. With nonuniform friction, slow rupture speed and small slip occur in a conditionally stable zone, while fast rupture speed and large slip mainly occur on asperities, forming multiple moment rate release peaks. In addition, discontinuous supershear rupture may occur near trench updip of asperities, but average rupture speed along the trench could be much lower, due to rupture slowing down effect from the conditionally stable zone. Low normal stress further contributes to slow moment release rate and exceptionally long normalized duration. Compliant hanging wall promotes cascade failure of multiple asperities to generate larger tsunami earthquakes and enhances shallow slip, thus increasing the tsunami potential.

In Model 5, the overall normal stress is lower than other models and could generate earthquakes with lower stress drops and longer normalized duration, consistent with observed features of historical tsunami earthquakes. Complex moment rate functions caused by asperities have been widely observed in tsunami earthquakes and numerous shallow subduction zone earthquakes (Bilek *et al*., 2004). An overall low effective normal stress could make the fault plane more heterogeneous. For example, if the average effective normal stress is 20 MPa in the conditionally stable zone, then a patch with higher normal stress of 50 MPa (30 MPa higher) will reduce h* on it to be 40% of that in the surrounding area and thus becomes more unstable, assuming all other parameters in equation (3) $a-b,\ L,\ \mu$ are the same. On the other hand, if the effective normal stress is 100MPa in the conditionally stable zone, then a patch with normal stress of 130 MPa (still 30 MPa higher) only reduces h* to be about 77% compared with the surrounding area. This may help explain why the source time functions of shallow subduction zone earthquakes, including tsunami earthquakes, are more complex compared with deeper earthquakes (Bilek *et al*., 2004).

In our models, we mainly compare the influence of heterogeneous fault friction and heterogeneous upper-plate velocity structure on tsunami earthquake generation and characteristics. Limited by computation needs of dynamic earthquake cycle simulations, we do not explore parameter spaces in detail by varying friction parameters (e.g., *a-b* value and *L*), changing fault geometry/dimension or varying location of asperities. For example, if we separate two asperities further away in Models 3, 4 and 5, the normalized duration for the simulated events could be longer and become more comparable to the observed range of 9-23 s of historical tsunami earthquakes. The general slow rupture speed of <1.5 km/s in the conditionally stable zone is a proof of this possibility. In this study, the asperity depth is around 10 km and thus the simulated tsunami earthquakes have a centroid depth of 10 km, which generates near-trench fault slip and seafloor displacement of several meters in amplitude (in Model 5). If we set up asperities shallower, for example < 5km depth, we could expect much larger near-trench fault slip and seafloor displacement, due a compliant upper plate. Effects of the separation distance between asperities may be found in Meng *et al.* (2022). We remark that, in addition to fault friction and upper-plate elastic properties, other factors such as the potential plastic yielding in the accretionary prism may also slow down rupture propagation and generate large seafloor displacement (Ma, 2012; Ma and Kirakawa, 2013). In the future, other potentially important factors should also be considered and systematically compared when studying specific tsunami earthquakes or over specific subduction zones.

In this study, we focus on studying the influence of fault friction and upper-plate rigidity on shallow tsunami earthquake characteristics. In a separate study, Kuo *et al*. (2022) use dynamic rupture modeling to examine roles of these two factors in depth-dependent rupture characteristics of large megathrust earthquakes that span the entire seismogenic zone. Their findings are consistent with our results obtained in this study, including (1) the dominate role of fault friction in slow rupture and high-frequency depletion at shallow depth and (2) the major contribution from the compliant upper-plate being enhanced near-trench slip.

6. Conclusions

In this study, we systematically compare contributions of heterogeneous fault friction and heterogeneous upper plate properties to tsunami earthquake generation and characteristics. Heterogeneous upper-plate properties are not sufficient to slow down ruptures to typical tsunami earthquake speed of <1.5 km/s over a large depth range (< 10 km). In contrast, heterogeneous fault friction distributions with asperities embedded in a conditionally stable zone can significantly slow down rupture speeds to be <1.5 km/s in the conditionally stable zone and generate long duration moment rate functions involving complex peaks, with spectra of low corner frequency and depleted high frequency energy. In addition, low effective normal stress on the subduction plane facilitates generating earthquakes with low stress drops and long normalized durations, consistent with the observed features of tsunami earthquakes. The depth dependent velocity structure with low rigidity at shallow depth mainly enhances large slip near trench and promotes cascading ruptures of multiple asperities in the conditionally stable zone. Tsunami earthquakes can happen at a centroid depth of 10 km, generating seafloor displacement with non-neglectable tsunami hazard. Our results show that heterogeneous fault friction provides a suitable environment for tsunami earthquake generation over a wide range of depth, playing a dominant role in tsunami earthquake characteristics.

Acknowledgements

This research is supported by NSF grant EAR-2147340. The authors appreciate Texas A&M High Performance Research Computing (https://hprc.tamu.edu) for providing the advanced computer resources used in this study.

References:

Abercrombie, R. E., M. Antolik, K. Felzer, and G. Ekström (2001), The 1994 Java tsunami earthquake: Slip over a subducting seamount, *J. Geophys. Res.*, 106, 6595–6607, doi:10.1029/2000JB900403.

Ammon, C. J., H. Kanamori, T. Lay, and A. A. Velasco (2006), The 17 July 2006 Java tsunami earthquake, *Geophys. Res. Lett.*, 33, L24308, doi:10.1029/2006GL028005.

Bassett, D., Sutherland, R. & Henrys, S. (2014), Slow wavespeeds and fluid overpressure in a region of shallow geodetic locking and slow slip, Hikurangi subduction margin, New Zealand. Earth Planet. Sci. Lett. 389, 1–13.

Bilek, S. L., and E. R. Engdahl (2007), Rupture characterization and aftershock relocations for the 1994 and 2006 tsunami earthquakes in the Java subduction zone, *Geophys. Res. Lett.*, 34, L20311, doi:10.1029/2007GL031357.

Bilek, S.L., Lay, T. (1999). Rigidity variations with depth along interplate megathrust faults in subduction zones. Nature 400, 443–446.. doi:10.1038/22739

Bilek, S.L., Lay, T. (2002), Tsunami earthquakes possibly widespread manifestations of frictional conditional stability. *Geophysical Research Letters* 29, 18-1-18-4.. doi:10.1029/2002gl015215

Bilek, S.L., Lay, T., Ruff, L.J., 2004. Radiated seismic energy and earthquake source duration variations from teleseismic source time functions for shallow subduction zone thrust earthquakes. Journal of Geophysical Research 109, n/a–n/a.. doi:10.1029/2004jb003039

Bizzarri, A., & Das, S. (2012). Mechanics of 3-D shear cracks between Rayleigh and shear wave rupture speeds. *Earth and Planetary Science Letters*, *357-358*, 397-404. https://doi.org/10.1016/j.epsl.2012.09.053

Chen, T., and N. Lapusta (2009), Scaling of small repeating earthquakes explained by interaction of seismic and aseismic slip in a rate and state fault model, J. Geophys. Res. Solid Earth, 114(B1), doi:10.1029/2008JB005749.

Contreras-Reyes, E., Maksymowicz, A., Lange, D., Grevemeyer, I., Muñoz-Linford, P., & Moscoso, E. (2017). On the relationship between structure, morphology and large coseismic slip: A case study of the Mw 8.8 Maule, Chile 2010 earthquake. *Earth and Planetary Science Letters*, *478*, 27–39. https://doi.org/10.1016/j.epsl.2017.08.028

Dieterich, J.H., Richards-Dinger, K.B., 2010. Earthquake Recurrence in Simulated Fault Systems, in: . pp. 233–250.. doi:10.1007/978-3-0346-0500-7_15.

Duan, B. (2010), Role of initial stress rotations in rupture dynamics and ground motion: A case study with implications for the Wenchuan earthquake, J. Geophys. Res. Solid Earth, 115(B5), doi:10.1029/2009JB006750.

Duan, B. (2012), Dynamic rupture of the 2011 Mw 9.0 Tohoku-Oki earthquake: Roles of a possible subducting seamount, J. Geophys. Res., 117(B5), doi:10.1029/2011JB009124.

Duan, B., and S. M. Day (2008), Inelastic strain distribution and seismic radiation from rupture of a fault kink, J. Geophys. Res., 113(B12), doi:10.1029/2008JB005847.

Duan, B., and D. D. Oglesby (2006), Heterogeneous fa 734 ult stresses from previous earthquakes and the effect on dynamics of parallel strike-slip faults, J. Geophys. Res., 111(B5), doi:10.1029/2005JB004138.

Houston, H., H. M. Benz, and J. E. Vidale, Time functions of deep earth- quakes from broadband and short period stacks, J. Geophys. Res., 103, 29,895–29,913, 1998.

Hughes, T. J. (2000), The Finite Element Method: Linear Static and Dynamic Finite Element Analysis, Courier Corporation.

Hyndman, R. D., Yamano, M., & Oleskevich, D. A. (1997). The seismogenic zone of subduction thrust faults. Island Arc, 6(3), 244–260.

Hyndman, R. D., & Wang, K. (1993). Thermal constraints on the zone of major thrust earthquake failure: The Cascadia subduction zone. Journal of Geophysical Research: Solid Earth, 98(B2), 2039–2060.

Ihmle´, P. F., J. M. Gomez, P. Heinrich, and S. Guibourg (1998), The 1996 Peru tsunamigenic earthquake: Broadband source process, Geophys. Res. Lett., 25, 2691– 2694.

Kanamori, H. (1972), Mechanism of tsunami earthquakes, Phys. Earth Planet. Inter., 6, 346–359, doi:10.1016/0031-9201(72)90058-1.

Kanamori, H., & Anderson, L. (1975). Theoretical basis of some empirical relations in seismology. *Bulletin of the Seismological Society of America*, **65**, 1073–1095.

Kanamori, H., and M. Kikuchi (1993), The 1992 Nicaragua earthquake: A slow tsunami earthquake associated with subducted sediments, Nature, 361, 714–716, doi:10.1038/361714a0.

Kitajima, H. & Saffer, D. M. (2012), Elevated pore pressure and anomalously low stress in regions of low frequency earthquakes along the Nankai Trough. Geophys. Res. Lett. 39, L23301.

Kimura, G., S. Hina, Y. Hamada, J. Kameda, T. Tsuji, M. Kinoshita, and A. Yamaguchi (2012), Runaway slip to the trench due to rupture of highly pressurized megathrust beneath the middle trench slope: The tsunamigenesis of the 2011 Tohoku earthquake off the east coast of northern Japan, Earth Planet. Sci. Lett., 339–340, 32–45, doi:10.1016/j.epsl.2012.04.002

Lapusta, N., and Y. Liu (2009), Three-dimensional boundary integral modeling of spontaneous earthquake sequences and aseismic slip, J. Geophys. Res. Solid Earth, 114(B9), doi:10.1029/2008JB005934.

Lapusta, N., Rice, J. R., Ben-Zion, Y., & Zheng, G. (2000). Elastodynamic analysis for slow tectonic loading with spontaneous rupture episodes on faults with rate- and state-dependent friction. *Journal of Geophysical Research: Solid Earth*, *105*(B10), 23765-23789. https://doi.org/10.1029/2000jb900250

Lay, T., Ammon, C. J., Kanamori, H., Yamazaki, Y., Cheung, K. F., & Hutko, A. R. (2011). The 25 October 2010 Mentawai tsunami earthquake (Mw7.8) and the tsunami hazard presented by shallow megathrust ruptures. *Geophysical Research Letters*, *38*(6), n/a-n/a. https://doi.org/10.1029/2010gl046552

Liu, D., and B. Duan (2018), Scenario Earthquake and Ground-Motion Simulations in North China: Effects of Heterogeneous Fault Stress and 3D Basin Structure, Bull. Seismol. Soc. Am., doi:10.1785/0120170374.

Liu, Y., Rice, J.R. (2007). Spontaneous and triggered aseismic deformation transients in a subduction fault model. Journal of Geophysical Research 112.. doi:10.1029/2007jb004930

Luo, B., and B. Duan (2018), Dynamics of Non-planar Thrust Faults Governed by Various Friction Laws, J. Geophys. Res. Solid Earth, doi:10.1029/2017JB015320.

Luo, B., Duan, B., and Liu, D. (2020), 3D Finite-Element Modeling of Dynamic Rupture and Aseismic Slip over Earthquake Cycles on Geometrically Complex Faults. Bulletin of the Seismological Society of America, 110, 2619–2637, doi:10.1785/0120200047.

Ma, S. (2012). A self-consistent mechanism for slow dynamic deformation and tsunami generation for earthquakes in the shallow subduction zone. Geophysical Research Letters, 39(11), L11310.

Ma, S., and Hirakawa, E. T. (2013), Dynamic wedge failure reveals anomalous energy radiation of shallow subduction earthquakes. Earth and Planetary Science Letters, 375, 113-122.

Meng, Q., Duan, B., Luo, B. (2022). Using a dynamic earthquake simulator to explore tsunami earthquake generation. Geophysical Journal International 229, 255–273.. doi:10.1093/gji/ggab470

Pelayo, A. M., & Wiens, D. A. (1992). Tsunami earthquakes: Slow thrust-faulting events in the accretionary wedge. *Journal of Geophysical Research*, *97*(B11). https://doi.org/10.1029/92jb01305

Prada, M., Galvez, P., Ampuero, J. P., Sallarès, V., Sánchez-Linares, C., Macías, J., & Peter, D. (2021). The Influence of Depth-Varying Elastic Properties of the Upper Plate on Megathrust Earthquake Rupture Dynamics and Tsunamigenesis. *Journal of Geophysical Research: Solid Earth*, *126*(11). https://doi.org/10.1029/2021jb022328

Qiang, S. (1988), An adaptive dynamic relaxation method for nonlinear problems, Computers &Structures, 30(4), 855-859.

Rubin, A.M., and Ampuero, J.-P. (2005). Earthquake nucleation on (aging) rate and state faults. Journal of Geophysical Research: Atmospheres 110.. doi:10.1029/2005jb003686.

Saffer, D.M., Lockner, D.A., Mckiernan, A., 2012. Effects of smectite to illite transformation on the frictional strength and sliding stability of intact marine mudstones. Geophysical Research

Letters 39, n/a–n/a.. doi:10.1029/2012gl051761

Sallares, V., & Ranero, C. R. (2019). Upper-plate rigidity determines depth-varying rupture behaviour of megathrust earthquakes. *Nature*, *576*(7785), 96-101. https://doi.org/10.1038/s41586-019-1784-0

Scholz, C. H. (1998), Earthquakes and friction laws, Nature 391:37-42.

Vidale, J.E., Houston, H. (1993). The depth dependence of earthquake duration and implications for. rupture mechanisms. Nature 365, 45–47.. doi:10.1038/365045a0

Wang, C. (1980). Sediment subduction and frictional sliding in a subduction zone. Geology, 8(11), 530–533.

Tables and Figures

Table 1. Models 1-5 and their simulated dynamic event results

Models (friction & velocity)	Dynamic Phases (Ruptured asperities)	Slip weighted Stress Drop (MPa)	Normalized duration (s)	Mw
Model 1 (simple velocity model & uniform friction model)	D1	5.1	4.7	7.94
	D2	3.0	7.3	7.61
	D3	4.6	5.8	7.89
Model 2 (heterogeneous velocity model & uniform friction model)	D1	5.2	4.5	7.97
	D2	3.0	7.7	7.67
	D3	3.0	6.7	7.78
Model 3 (simple velocity model & nonuniform friction model)	D1 (Z1Z2)	2.9	9.8	7.68
	D2 (Z2)	2.6	11.6	7.32
	D3 (Z1)	3.0	8.4	7.58
	D4 (Z2)	2.4	13.3	7.30
Model 4 (heterogeneous velocity model & nonuniform friction)	D1 (Z1Z2)	3.0	7.7	7.71
	D2 (Z1Z2)	3.1	7.2	7.74
	D3 (Z1Z2)	3.0	7.2	7.73
Model 5 (heterogeneous velocity model & nonuniform friction with low normal stress)	D1 (Z1Z2)	1.7	10.6	7.51
	D2 (Z1Z2)	1.6	14.0	7.51
	D3 (Z1Z2)	1.6	10.6	7.52

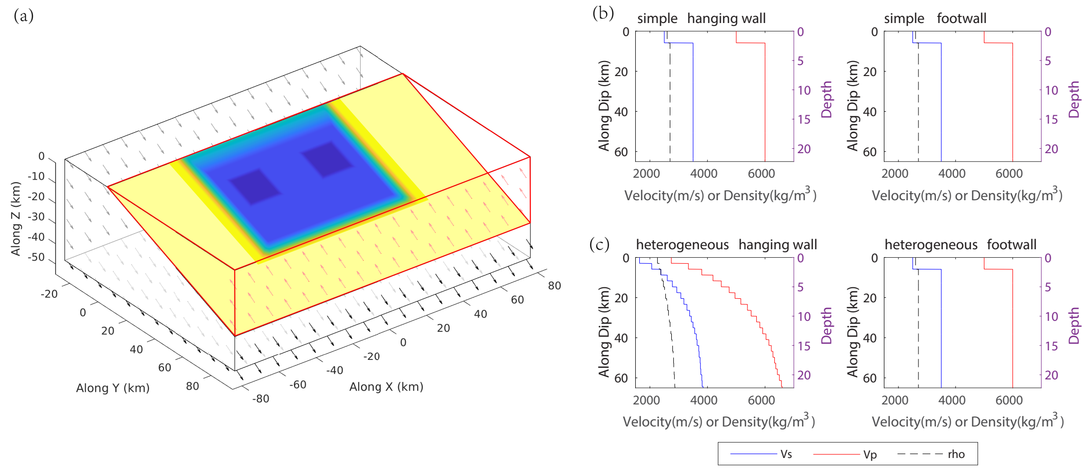

Figure 1. (a) Schematic diagram for fault geometry (a 20° dipping subduction plane) and boundary conditions of the models, with dimension of the model along *X* axis: Xmin (-80km) to Xmax (80km), along Y axis: Ymin (-30 km) to Ymax (80 km) and along *Z* axis: Zmin (-50 km) to Zmax (0 km). The main fault plane (blue) with a largely velocity-weakening frictional property that can host earthquake ruptures is surrounded by a velocity-strengthening area (yellow) that creeps. During the quasi-static phase, one half of the plate convergence rate ($0.5*10^{-9}$m/s) parallel with the fault plane is applied upward (red arrows at the boundary Y=Ymax) on hanging wall (outlined by red frame) and downward (black arrows at boundaries Y=Ymax, Y=Ymin and Z=Zmin) on footwall wall (outlined by black frame). (b) The simple velocity model that both the hanging wall and footwall use the same two-layer velocity structure, where *Vp*=5.0 km/s and *Vs*= 2.5km/s at the top layer (<2km) and *Vp*=6.0km/s and *Vs*=3.5km/s at the bottom layer. (c) Heterogeneous velocity model that the hanging wall uses a depth varying velocity structure (Sallares and Ranero, 2019) with low velocity near shallow depth, where *Vp*=2.7 km/s and *Vs*=1.6 km/s near the trench, and the footwall uses a two-layer velocity structure as the simple velocity model, shown in (b).

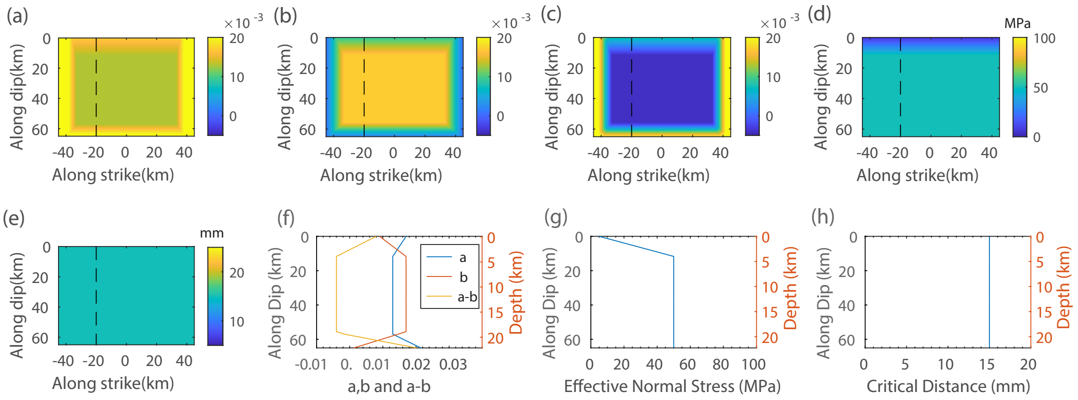

Figure 2. The on-fault parameters for the uniform friction model (in Models 1 and 2): distributions of friction parameters (a) *a*, (b) *b*, (c) *a-b*, (d) effective normal stress and (e) critical distance over the fault plane; the cross sections of friction parameters (f) *a*, *b*, *a-b,* (g) effective normal stress, and (h) critical distance along a dip profile (the dashed lines in (a)-(e)). The fault is velocity strengthening near the trench (*a-b*=0.008 at 0km depth) and quickly transitions to velocity weakening (*a-b*=-0.004 at depth =4 km) and stay uniform over most of the fault plane, then transitions to velocity strengthening at bottom of the main fault plane (*a-b*=0.02), as shown in (f).The effective normal stress near trench (depth 0 km) is 5MPa and linearly increases to 50 MPa at depth of 4km and keeps uniform over most of the fault plane, as shown in (g).

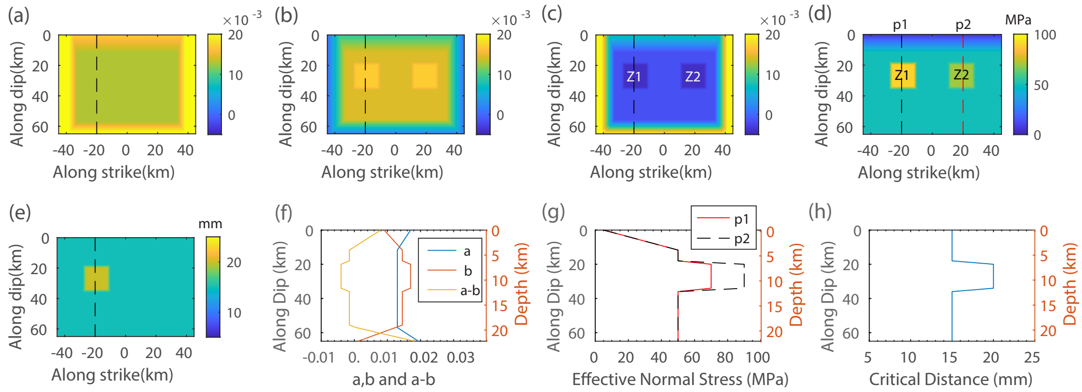

Figure 3. The on-fault parameters for the nonuniform friction model (in Models 3 and 4): distributions of friction parameters (a) *a*, (b) *b*, (c) *a-b*, (d) effective normal stress and (e) critical distance over the fault plane; the cross sections of friction parameters (f) *a*, *b*, *a-b*, (g) effective normal stress, and (h) critical distance along a dip profile (the dashed lines in (a)-(e)). The two normal stress cross sections p1 and p2 in (g) pass through two asperities Z1 and Z2 shown in (d). The fault is velocity strengthening near the trench (*a-b*=0.008 at 0km depth) and quickly transitions to conditionally stable (*a-b*=-0.0015 at depth =4 km) and stay uniform over most of the fault plane below 4 km, then transitions to velocity strengthening at bottom of the main fault plane (*a-b*=0.02), as shown in (f). On two asperities Z1 and Z2, the *a-b* equals -0.004 and represents strongly velocity weakening friction property. The effective normal stress near trench (depth 0 km) is 5MPa and linearly changes to 50 MPa at depth of 4km and keeps uniform over most of the fault plane, as shown in (g). On asperity Z1 normal stress is 90 MPa and on Z2 is 70 MPa. Critical distance is 15 mm over most of the fault plane, while on Z1 is 20 mm.

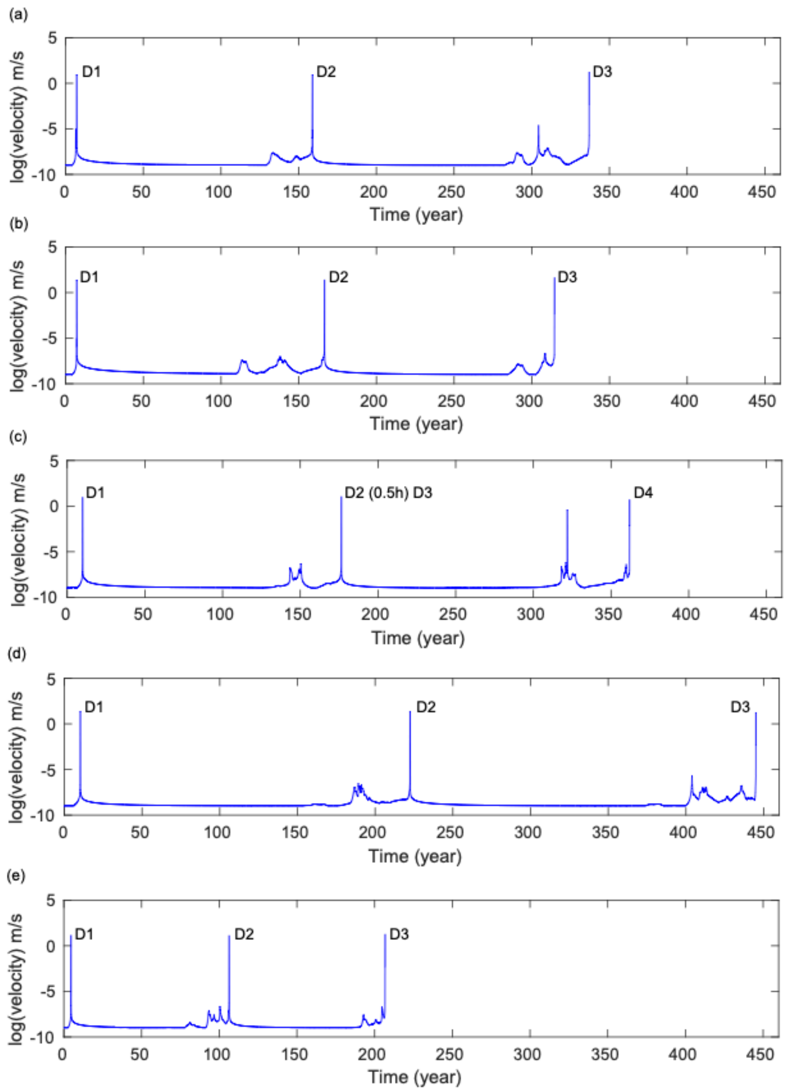

Figure 4. The simulated maximum slip rate on the fault over earthquake cycles, for (a) Model 1, (b) Model 2, (c) Model 3, (d) Model 4, (e) Model 5. The high slip rate peaks (~1 m/s or larger) represent dynamic events and the time (about 100-200 of years) between two dynamic events is the earthquake recurrence interval, except in (c), where two dynamic events (D2 and D3) occurring on the two asperities separately with 0.5 hour delay may be considered as one clusterred event.

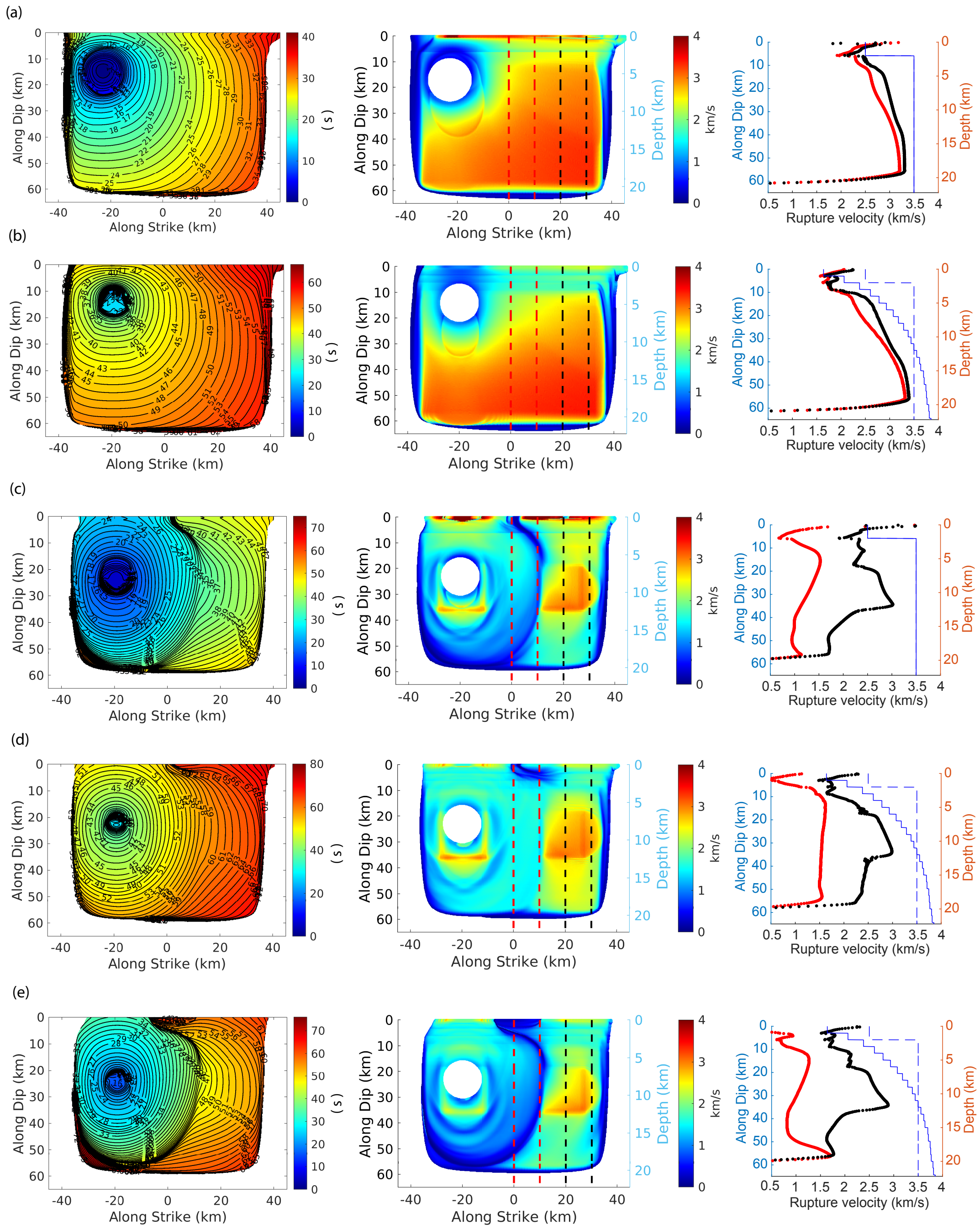

Figure 5. The rupture contour (left column), rupture speed distribution (middle column) and rupture speed profiles (right column), for (a) D1 in Model 1, (b) D1 in Model 2, (c) D1 in Model 3, (d) D1 in Model 4, and (e) D1 in Model 5. For the rupture speed profiles (right column), the red velocity profile shows the average rupture speed of each depth over a narrow zone outlined by two dashed red lines in the rupture speed panels (middle column); and the black velocity profile corresponds to

the average rupture speed within the two black dashed lines in the rupture speed panels (middle column). The blue solid line and dashed line represent the *Vs* velocity of the hanging wall and footwall for comparison.

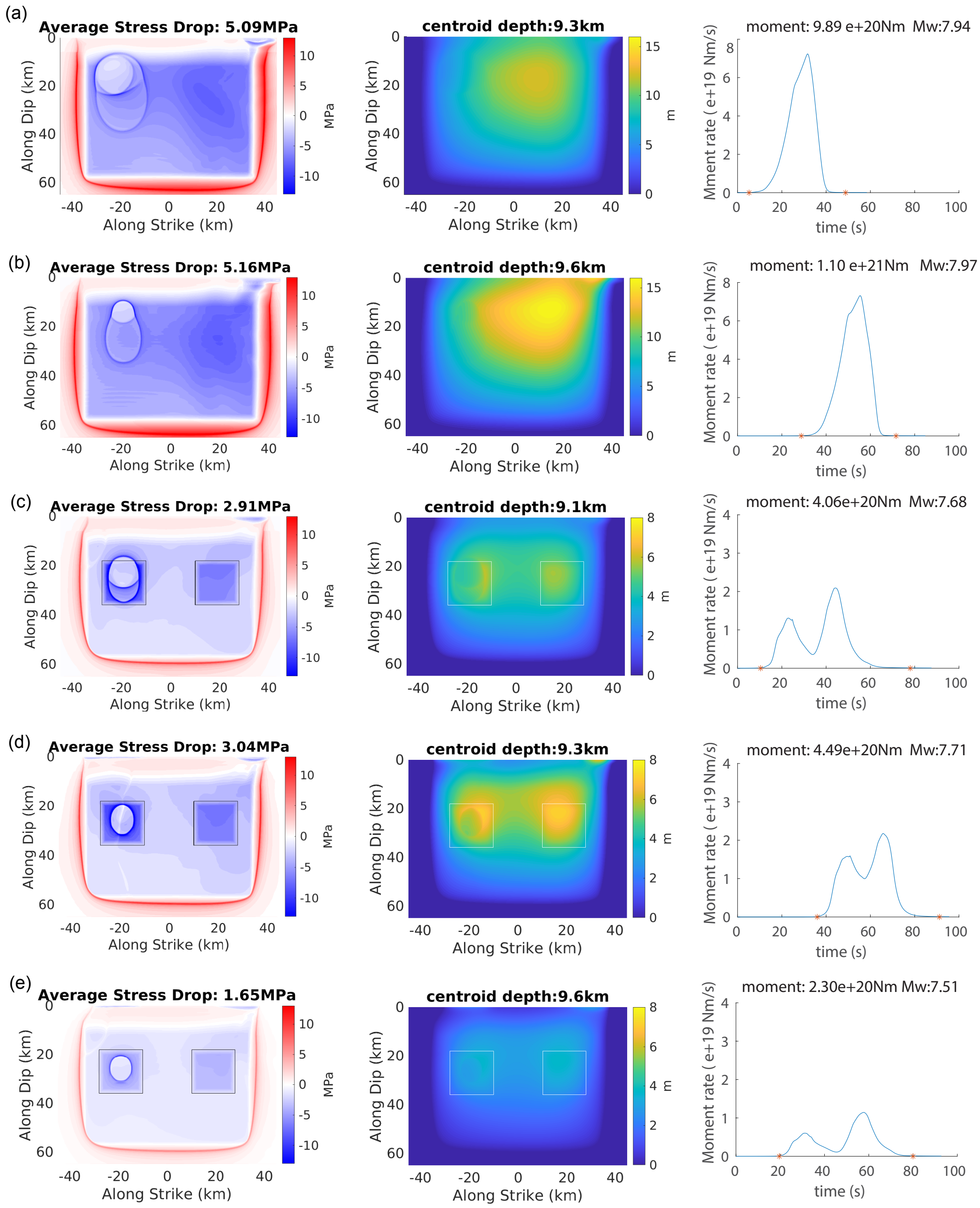

Figure 6. The stress change distribution (left column), final slip distribution (middle column) and

moment rate function, for (a) D1 in Model 1, (b) D1 in Model 2, (c) D1 in Model 3, (d) D1 in Model 4, and (e) D1 in Model 5. The black and white boxes in stress change and final slip panels in (c) (d) (e) represent the locations of two asperities in Models 3-5 with nonuniform friction parameters. The scales of slip and moment rate in (a) (b) are different with those in (c) (d) (e), though the scale of stress changes is the same. Two red stars (10^{17} Nm) on the moment rate functions (right column) denote the starting and ending times used to measure source durations T.

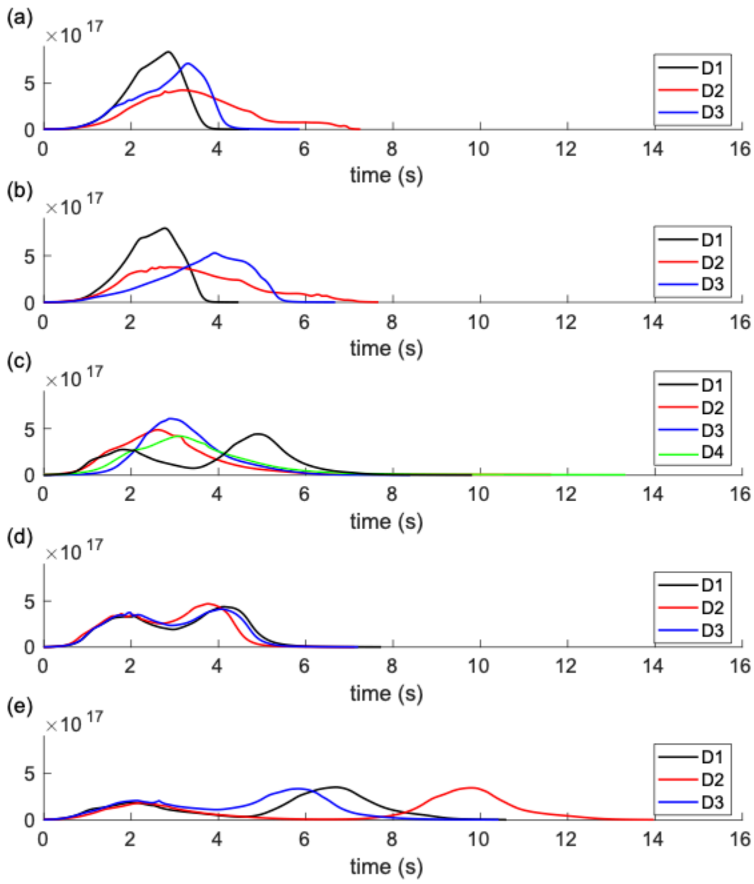

Figure 7. The normalized moment rate functions for all dynamic events simulated in (a) Model 1, (b) Model 2, (c) Model 3, (d) Model 4, (e) Model 5.

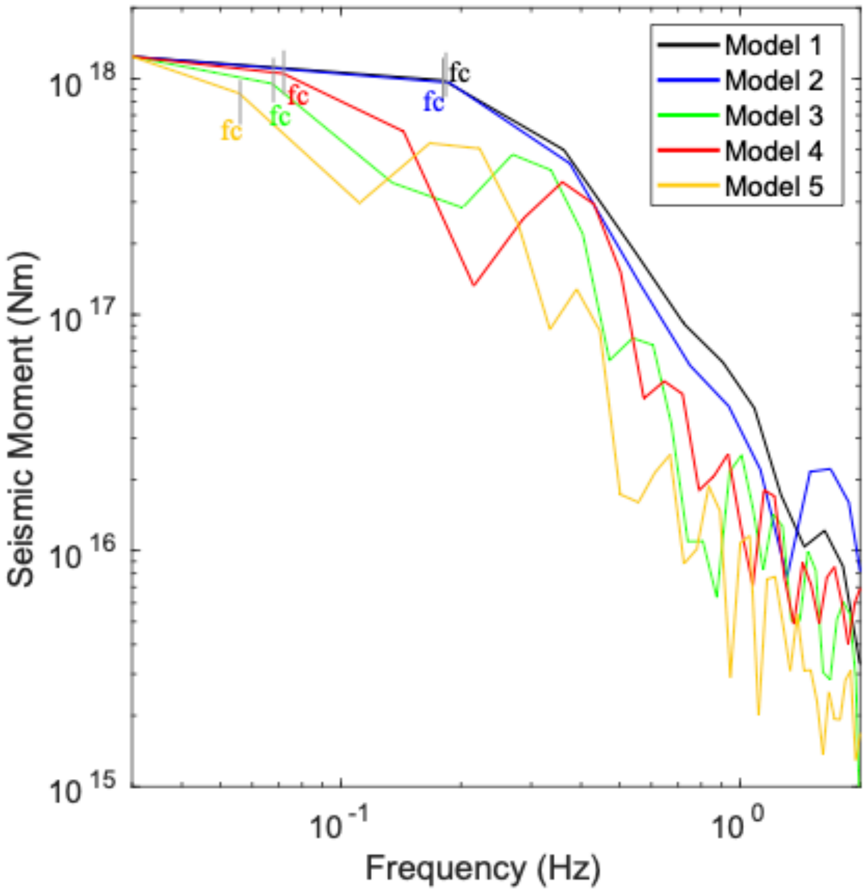

Figure 8. The spectra for the normalized moment rate functions of event D1 in Model 1 (black), Model 2 (blue), Model 3 (green), Model 4 (red) and Model 5 (orange). The normalized moment rate functions are shown in Fig. 7. The vertical bars demonstrate the corner frequencies.

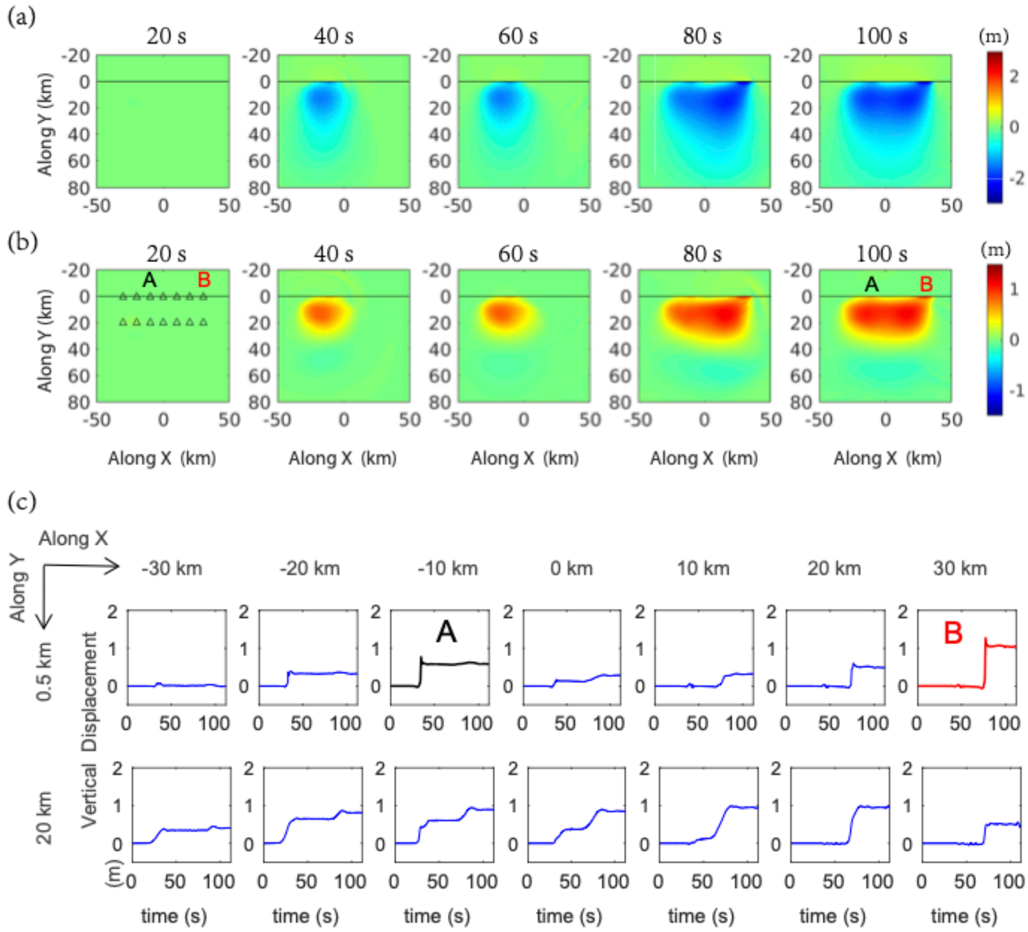

Figure 9. The snapshots of (a) horizontal displacement along Y axis (perpendicular to the trench) and (b) vertical displacement along *Z* axis at 20s, 40s, 60s,80s and 100s of event D2 in Model 5, and (c) time histories of vertical displacement at an virtual array of seafloor stations shown by triangles in (b).